

Microstructural evolution of a model, shear-banding micellar solution during shear startup and cessation

Carlos R. López-Barrón,¹ A. Kate Gurnon,² Aaron P. R. Eberle,³ Lionel Porcar,⁴ and Norman J. Wagner^{2,*}

¹*ExxonMobil Chemical Company, Baytown, Texas 77520, USA*

²*Center for Neutron Science, Department of Chemical & Biomolecular Engineering, University of Delaware, Newark, Delaware 19716, USA*

³*Center for Neutron Research, National Institute of Standards and Technology, Gaithersburg, Maryland 20899, USA*

⁴*Institut Laue-Langevin, BP 156, F-38042 Grenoble Cedex 9, France*

(Received 15 July 2013; published 10 April 2014)

We present direct measurements of the evolution of the segmental-level microstructure of a stable shear-banding polymerlike micelle solution during flow startup and cessation in the plane of flow. These measurements provide a definitive, quantitative microstructural understanding of the stages observed during flow startup: an initial elastic response with limited alignment that yields with a large stress overshoot to a homogeneous flow with associated micellar alignment that persists for approximately three relaxation times. This transient is followed by a shear (kink) band formation with a flow-aligned low-viscosity band that exhibits shear-induced concentration fluctuations and coexists with a nearly isotropic band of homogenous, highly viscoelastic micellar solution. Stable, steady banding flow is achieved only after approximately two reptation times. Flow cessation from this shear-banded state is also found to be nontrivial, exhibiting an initial fast relaxation with only minor structural relaxation, followed by a slower relaxation of the aligned micellar fluid with the equilibrium fluid's characteristic relaxation time. These measurements resolve a controversy in the literature surrounding the mechanism of shear banding in entangled wormlike micelles and, by means of comparison to existing literature, provide further insights into the mechanisms driving shear-banding instabilities in related systems. The methods and instrumentation described should find broad use in exploring complex fluid rheology and testing microstructure-based constitutive equations.

DOI: [10.1103/PhysRevE.89.042301](https://doi.org/10.1103/PhysRevE.89.042301)

PACS number(s): 83.80.Qr, 47.57.Qk, 61.05.fg, 83.80.Rs

I. INTRODUCTION

A broad interest in material instabilities under deformation exists across many fields of science, including solids, complex fluids, and granular materials [1]. Startup flows have proven to be particularly valuable for the study of such instabilities [2–5]. A model system of particular focus is the shear-banding flow of self-assembled surfactant polymerlike micelles (PLMs) or wormlike micelles (WLMs) [6,7]. One aspect that makes these complex fluids so intriguing and technologically important is that shear-banding PLMs exhibit an apparent stress plateau in their steady-state flow curve over a wide range of shear rates $\dot{\gamma}_{1c} < \dot{\gamma} < \dot{\gamma}_{2c}$ (Fig. 1) [6,8]. When a stress corresponding to the plateau is applied to long, threadlike micelles in a Couette geometry, the fluid is organized into two coexisting bands: a low-viscosity birefringent band flowing at $\dot{\gamma}_{2c}$, near the inner rotating cylinder, and a nearly isotropic band, flowing at $\dot{\gamma}_{1c}$, near the outer stationary wall [9–12]. These birefringent and isotropic bands have been presumed to be (shear-aligned) disentangled and entangled phases, respectively [4,10,11,13], although arguments have been put forth for nematic formation in the high-shear band [14]. On the other hand, for highly branched PLMs shear banding is a consequence of shear-induced demixing [15–17], while for micellar systems with compositions near an isotropic-nematic phase transition, shear banding is due to flow-induced nematic formation [13,18,19]. However, modeling of the shear-banding condition involves a nonmonotonic constitutive equation that leads to shear flow instability between $\dot{\gamma}_{1c}$ and $\dot{\gamma}_{2c}$ that may or may not be coupled with underlying thermodynamic phase transitions

or shear-induced demixing [20–23]. Finally, we note that highly viscoelastic PLMs may show unsteady or chaotic shear banding [20,24].

Significant advances in our understanding of shear banding have resulted from advances in experimental methods that measure the nonhomogeneous velocity field [e.g., particle image velocimetry (PIV) [4,25] and NMR [26,27]] and the state of aggregation and alignment of the micelles [e.g., flow-induced birefringence (FIB) [12,28,29], small-angle light scattering (SALS), [4,17] and small-angle neutron scattering (SANS) under flow [16,19]], as well as advanced constitutive modeling [30–32]. These methods have been reviewed recently [33]. However, a definitive understanding of shear banding requires understanding the underlying microstructure responsible for the stress and the mechanism that selects the location of the stress plateau. This in turn necessitates spatially and temporally resolved quantitative measurements of the flow field and, as importantly, quantitative measurements of *the local microstructure under flow*. Here we present quantitative measurements of the microstructure in the plane of flow with spatial and temporal resolution, enabled by means of SANS sample environments and methods [34,35].

Transient flows such as startup of shear flow provide an avenue for probing the kinetics of shear banding and the nature of the underlying flow field [3]. Hu *et al.* identified sequential evolution of PLM microstructure in Couette flow during startup at shear rates well into the stress plateau [4,25]: a stress overshoot on a relatively short time scale that is typical of an elastic response with wall slip, followed by a relatively long-lived metastable state with a homogeneous flow typical of a shear-thinning material that slowly segregates into a steady-kink shear-banding state. Similar measurements in a wide gap Couette device by Miller and Rothstein [28] also illustrate this

*wagnernj@udel.edu

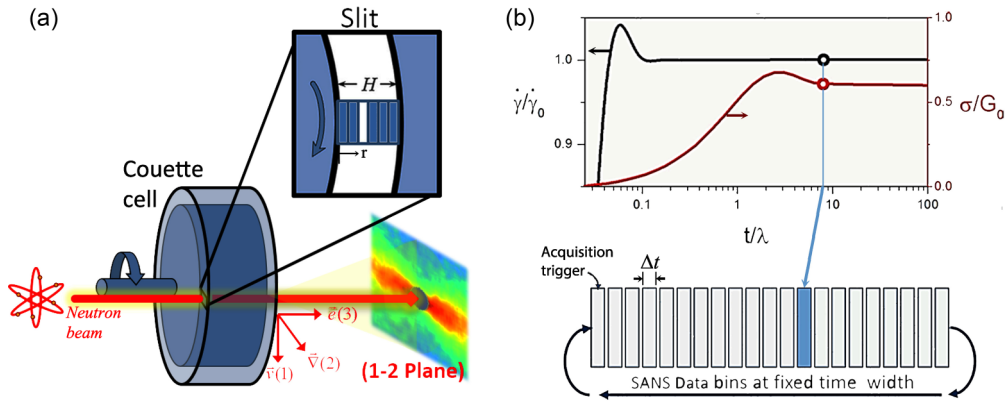


FIG. 1. (Color online) (a) Schematic diagram of the 1-2 Couette flow cell. Space resolution is provided by the slit. (b) Schematic representation of the synchronization of the SANS data collection with the transient deformation applied in the rheometer. The indicated cycle is repeated until statistically significant scattering is collected at each time bin.

general sequence and add flow-birefringence measurements that confirm the difference in alignment between the low- and high-shear bands [8, 11, 12, 29, 36]. Miller and Rothstein also reported an initial birefringence overshoot, occurring at times on the order of λ (where λ is the relaxation time), suggesting early dynamics connected to the velocity profile development. Hu and Lips also report a strong transient flow-SALS “butterfly” pattern in both bands at the transition from the metastable state to the onset of shear banding that eventually fades in the outer band but strengthens in the inner band as the banded velocity profile matures [4]. They hypothesize a sequence of underlying PLM microstructure transitions, where the highly entangled, isotropic structure undergoes an initial disentanglement with nearly-rate-independent stress (elastoplastic behavior) until, after an initial stress overshoot, it flows as typical for a shear thinning polymer solution. This homogeneous, transient behavior, which is also evident as an induction period in stress-controlled startup flows, then evolves to a kink shear-banded state as suggested by modeling [31].

The formation of stable shear bands proceeds by the outer shear band lowering its characteristic shear rate to $\dot{\gamma}_{1c}$ and the PLM in this band is presupposed to reentangle and thereby increase viscosity. The inner shear band evolves to flow at rates comparable to $\dot{\gamma}_{2c}$, but with large concentration fluctuations evident in SALS, along with significant flow birefringence. As noted by Hu *et al.*, this hypothesis for microstructure evolution is in contradiction to the prior prevailing hypothesis proposed by Berret [14] that shear banding proceeds by the nucleation and growth of a nematic phase near the inner rotating cylinder. Berret studied a surfactant solution of the same chemical composition as that analyzed by Hu *et al.* (cetylpyridinium chloride and sodium salicylate diluted in 0.5M NaCl brine), but with higher composition (Berret’s solution composition is 12%, whereas the Hu *et al.* solution is 5.9%). However, both concentrations lie in the semidilute concentration regime, between the overlap concentration (3%) and far from the isotropic-nematic phase boundary (36%) [14]. Although Hu *et al.* provide substantial arguments in favor of their proposed scenario, to date direct measurements capable of quantitatively testing and resolving this disagreement are lacking.

More generally in the field of complex fluids, the aforementioned studies illustrate how the rich rheological transient

response upon flow startup can coincide with the development of inhomogeneous flow fields that are presupposed to be due to spatial and temporal microstructural changes, as inferred from rheology, PIV, SALS, and FIB. However, to date, quantitative measurements on the state of aggregation, alignment, and orientation of model complex fluids during startup flow that can confirm this causality are lacking. Such information is crucial for rigorous validation of constitutive models that couple the spatiotemporal evolutions of both microstructure (e.g., number density and conformation of active species) and the velocity field [30–32, 37, 38]. Here we report direct local measurements of the evolution of the segmental-level microstructure of a shear-banding PLM solution during startup of shear and subsequent relaxation after flow cessation.

II. EXPERIMENT

A. Materials

The micellar solution studied in this work is a 6 wt. % cetylpyridinium chloride (CPCL) (5.16 wt. % of CPCL monohydrate)/sodium salicylate (1.12 wt. %) ([NaSal]/[CPyCl] = 0.5) dissolved in 0.5M NaCl D₂O brine (this is a similar composition to that of Hu and Lips, 7.3 wt. %, but their formulation is in H₂O) [4] at 25 °C [8, 14, 39]. This composition is a viscoelastic solution with nearly Maxwellian behavior (plateau modulus $G_0 = 103.2$ Pa and relaxation time $\lambda = 0.42$ s) (see Fig. S1 in the Supplemental Material [40]) and a threadlike-micellar microstructure. Here D₂O is used to enhance SANS contrast and the effects of isotope substitution have been documented [41].

B. Rheometry

Rheological measurements were performed at 25 °C on a TA Instruments ARES-G2 strain-controlled rheometer using a Peltier Couette geometry (with a bob diameter of 27.7 mm and a cup diameter of 30 mm) and a cone and plate geometry (with a diameter of 50 mm and angle of 0.04 rad). The linear viscoelastic (LVE), steady shear, and transient rheologies of the CPCL solution were measured using the following protocol: A preshear of 10 s⁻¹ for 60 s, followed by 120 s of rest, was applied to the sample to ensure homogenization. The LVE response was then measured by performing a frequency

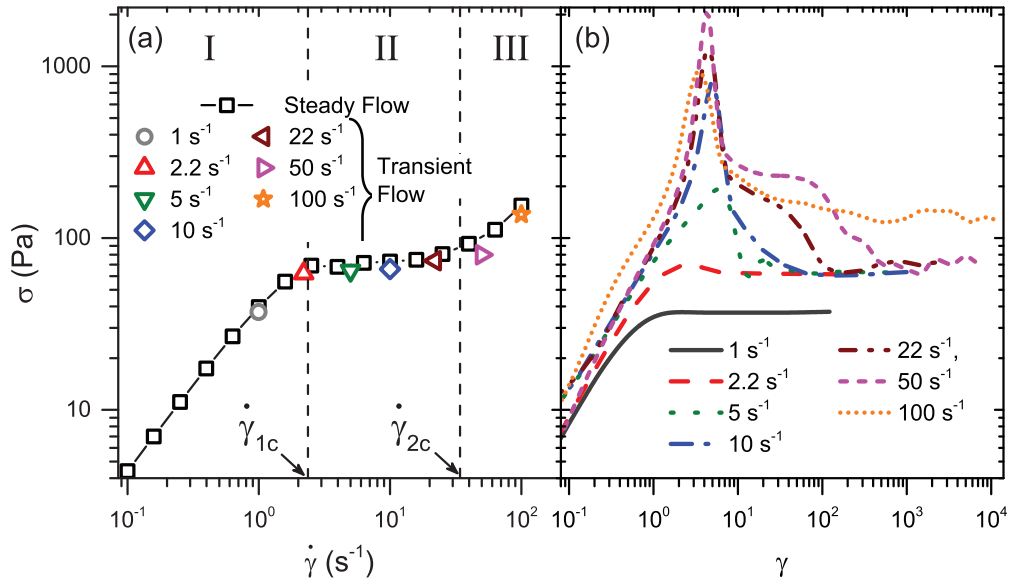


FIG. 2. (Color online) (a) Steady flow curve measured by increasing the ramp of the shear rate (black squares) and stress values measured at 60 s after the start of transient experiments (colored symbols). (b) Transient shear stress versus strain for shear startup as indicated in (a). Regions I–III are defined by the onset $\dot{\gamma}_{1c}$ and end $\dot{\gamma}_{2c}$ of shear-banding flow.

sweep from 0.2 to 200 rad/s using a strain amplitude of 5%. Subsequently, steady shear rate sweeps were performed in both Couette and cone-plate geometries from 0.1 to 100 s^{-1} to measure the steady shear rheology (flow curve). Equilibration time at each shear rate was 60 s and the stress was measured by sampling data for 30 s. Transient rheological response was measured by performing startup shear tests at selected shear rates using the cone-plate geometry.

C. Stroboscopic flow SANS in the 1-2 plane

The flow-aligned microstructure on the segmental length scale of the PLM is measured by a technique of spatial and temporal resolved small-angle neutron scattering under flow (1-2 spatiotemporal resolved flow SANS) [42]. Measurements in the velocity-velocity gradient ($\vec{v} - \vec{\nabla}v$) plane of shear are carried out using an aluminum short-gap Couette flow cell [depicted in Fig. 1(a)] described elsewhere [16]. A 0.1-mm slit (see Fig. 1) is used to translate the beam across the gap so as to enable probing coexisting bands in a shear-banding fluid. The relative gap position r/H of the center of the slit is referenced to the inner rotating cylinder ($r/H = 0$).

The 1-2 stroboscopic flow-SANS technique consists of stroboscopic synchronization of streaming SANS intensity with the start of transient shear deformation applied in the rheometer [35,43]. A diagram of the synchronization is depicted in Fig. 1(b) and a detailed description of the instrument and its operation, along with technical drawings of its construction, has been published recently [34]. The time-resolved experiments bin data into $n_b = T/\Delta t$ bins of Δt duration for a cycle time of T . The scattering intensity is collected over a prescribed number of repeated transient experiments n_c and summed to achieve sufficient total scattering intensity. The time resolution, defined by the noise in the analog signal that triggers the top-off event, is less than 1 ms. Here we use $n_c \approx 300$ and two different intervals for both the startup event (with $\Delta t_1 = 0.2$ s, $T_1 = 4$ s and $\Delta t_2 = 1$ s, $T_2 = 26$ s) and the relaxation

event (with $\Delta t_3 = 0.2$ s, $T_3 = 2$ s and $\Delta t_4 = 1$ s, $T_4 = 8$ s). A prerequisite for choosing a material to be interrogated with 1-2 stroboscopic flow SANS is that it behaves reproducibly for each subsequent transient event so that a sufficient number of cycles can be summed to collect statistically valid scattering patterns in each time bin. Here we validate that the sample fully recovers to equilibrium during the relaxation period. The method is implemented on the D22 SANS beam line (ILL, Grenoble, France). The incident neutron beam was aligned parallel to the vorticity direction \vec{e} and the scattering intensity represents the two-dimensional (2D) projection of the plane of shear [as shown in Fig. 1(a)]. Complementary rheo-SALS patterns are recorded in the plane orthogonal to the velocity gradient $\vec{\nabla}v$ in a parallel-plate geometry (TA Instruments DHR w/SALS) using a 1-mm gap described in detail in [17].

III. RESULTS AND DISCUSSION

A. Shear startup

The shear startup transient rheology and flow-SANS measurements are performed at two shear rates: The first is at the onset of the stress plateau, 2.2 s^{-1} , while the second is deep into the stress plateau, 22 s^{-1} , as indicated in Fig. 2. Figure 2(a) shows the steady shear stress as a function of shear rate for reference. Figure 2(b) shows how the stress evolves with strain during startup of shear flow. These experiments are plotted as a function of the shear strain to illustrate the common, elasticlike response expected for the nearly instantaneous startup flow of a highly entangled viscoelastic fluid, such as that probed here [3,25]. Significant stress overshoots and anomalously long transients are evident in the transient stress response [Fig. 2(b)] for rates that correspond to the stress plateau in the steady flow curve [Fig. 2(a)]. As previously reported [25,44], wall slip is evident in velocimetry measurements during the very early, elastic response, but is not present thereafter. These rich

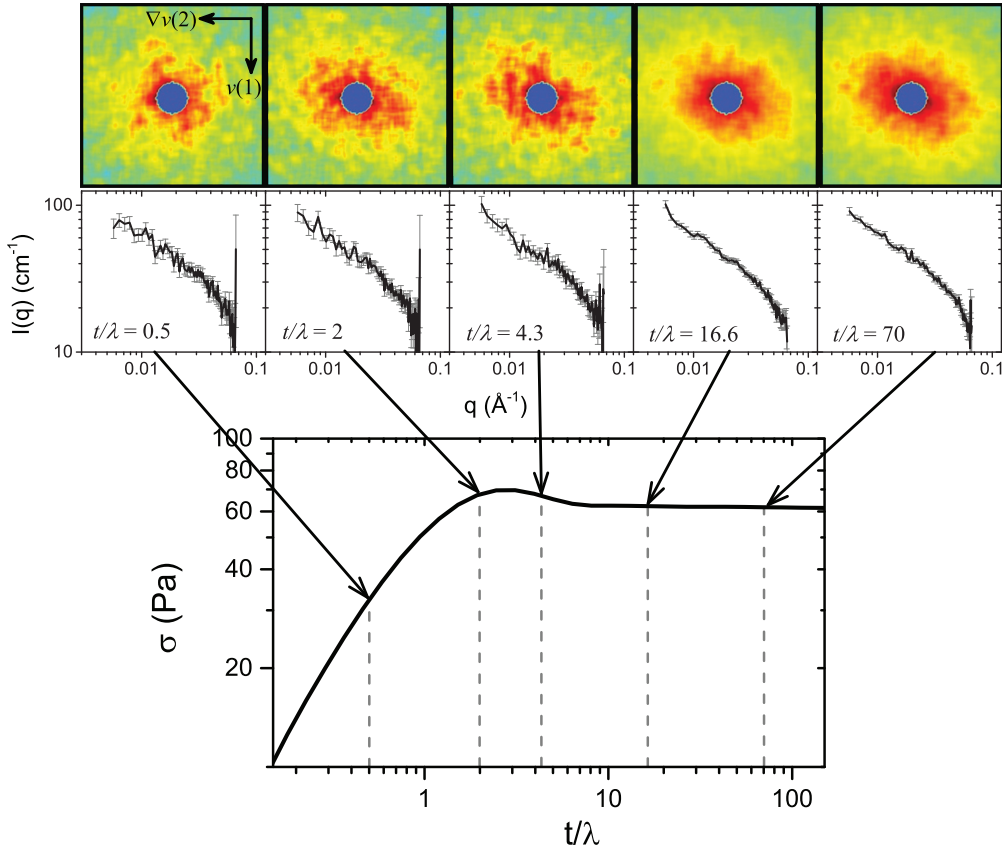


FIG. 3. (Color online) Shear startup with $\dot{\gamma} = 2.2 \text{ s}^{-1}$: The upper panel shows 2D SANS patterns in the $\vec{v} - \vec{\nabla}v$ (1-2) plane as indicated, measured at the times indicated by the arrows; the middle panel shows $\langle I(q,t) \rangle$ for these patterns; and the lower panel shows the shear stress versus time.

transients have been reported previously and are a topic of interest as they can provide important, new information about the underlying constitutive equation as well as being technologically significant. This complex rheological response provides indirect indication of the known complex temporal evolution of the underlying kinematics [25] and, as will be shown here, dramatic microstructural transitions that drive the phenomenon.

Small-angle neutron scattering measurements were performed at the gap position $r/H = 0.2$ for shear rate $\dot{\gamma} = 2.2 \text{ s}^{-1}$, which corresponds to region I [Fig. 2(a)], where the flow field is homogeneous. Figure 3 shows the 2D SANS spectra in the velocity (down, vertical) –velocity gradient (left, horizontal) plane of observation for select representative time points along the flow curve, along with the circularly averaged absolute scattering intensity $\langle I(q) \rangle$. A mild stress overshoot, at $t \sim 2.5\lambda$, is followed by a nearly monotonic decay to a plateau stress for $t > 10\lambda$. Only a mild distortion of the structure is observed in the scattering patterns and no significant distortion of the averaged intensity is observed, showing that the viscoelastic, entangled wormlike micellar network is only mildly shear oriented, as expected.

The flow-induced ordering of the micellar segments is quantified using a standard definition of an order parameter known as the alignment factor, defined as [45]

$$|A_f|(q^*) = \frac{\int_0^{2\pi} I(q^*, \phi) \cos[2(\phi - \phi_0)] d\phi}{\int_0^{2\pi} I(q^*) d\phi}, \quad (1)$$

where $I(q^*, \phi)$ is the annular-averaged scattered intensity further averaged over a q range q^* ($0.006 \text{ \AA}^{-1} < q < 0.03 \text{ \AA}^{-1}$). This range of scattering length corresponds to the *segmental length scale* of the PLM. Access to the 1-2 plane of flow enables determining the primary direction of segmental orientation relative to the flow ϕ_0 , where ϕ is the azimuthal angle with respect to the flow direction and ϕ_0 is the average segmental orientation given by the minimum in $I(q^*, \phi)$. Here $|A_f|$ is a measure of the degree of micellar alignment about ϕ_0 and values range from 0 for the isotropic state to ~ 0.7 for a typical nematic fluid [13].

Figures 4(a) and 4(b) show the measured shear stress and first normal stress difference (lines), while Figs. 4(c) and 4(d) show the transient values of $|A_f|$ and ϕ_0 during startup shear (symbols). For very early times ($t < 0.5\lambda$) the system is nearly isotropic. This isotropic entangled state coincides with the mild stress overshoot, indicating that the stress enhancement is due to rapid straining of the entangled network, similar to that observed for polymer melts and solutions [46]. The development of anisotropy in the SANS 2D patterns indicates micellar alignment, which starts to develop at $t \sim \lambda$. The characteristic order parameters $|A_f|$ and ϕ_0 are observed to reach extrema at $t > 2\lambda$. Here $|A_f|$ and ϕ_0 evolve in time smoothly to plateau values ($A_{f,\text{plateau}} = 0.072 \pm 0.011$ and $\phi_{0,\text{plateau}} = 21.7^\circ \pm 1.5^\circ$) without further structural changes for $t > 10\lambda$.

These unique measurements of the microstructure in the plane of flow enable a quantitative comparison between the

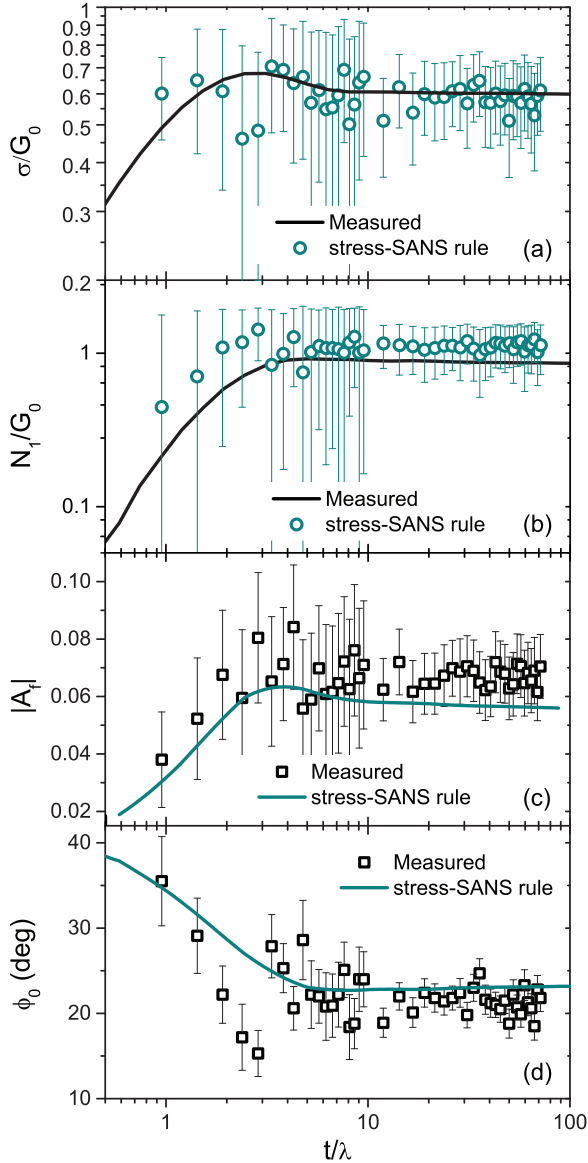


FIG. 4. (Color online) Shear startup with $\dot{\gamma} = 2.2 \text{ s}^{-1}$: (a) stress response and (b) first normal stress difference. In (a) and (b) the measured rheology (solid line) is compared to that calculated (symbols) via the stress-SANS rule and measured data of $|A_f|$ and ϕ_0 , given in (c) and (d), respectively. Solid lines in (c) and (d) are predictions using the stress-SANS rule and measured values of σ and N_1 .

microstructure and measured shear stress for flow startup. Based on the fact that both A_f and ϕ_0 represent two independent scalar parametrizations of the orientation order tensor (which describe the orientation conformation of the chains relative to the quiescent state) in the 1-2 plane, Helgeson *et al.* showed that the polymeric contributions to rheological material functions follow a stress-SANS rule [13], which is analogous to the stress-optic rule. The symbols in Figs. 4(a) and 4(b) show the stress computed with the stress-SANS rule, whose functional form for the stress and first normal stress difference are given as [13]

$$\sigma = G_0[C_1(\dot{\gamma})A_f]^{1/2}\sin(2\phi_0), \quad (2)$$

$$N_1 = 2G_0[C_1(\dot{\gamma})A_f]^{1/2}\cos(2\phi_0). \quad (3)$$

Steady shear measurements reported elsewhere [47] are used to define the stress-SANS rule coefficient $C_1 = 11.2$ for $\dot{\gamma} < \dot{\gamma}_{1c}$. As seen, excellent quantitative agreement is observed for this sample flowing homogeneously with only weak flow alignment, showing that there is a direct quantitative correspondence between the segmental microstructure and the rheology, as expected, which serves to validate the experiment.

The transient behavior and the relationship between the stress and microstructure is much more complicated for startup of shear flow at 22 s^{-1} , which corresponds to a shear-banding state well into the stress plateau for steady shear flow [Fig. 2(a)]. Figure 5 shows the transient stress, 2D SANS profiles, and circularly averaged SANS intensities. The scattering measurements are reported for two locations in the gap ($r/H = 0.2$ and 0.8), which correspond to locations in the high and low-shear bands at steady state, respectively. A very pronounced overshoot is observed in both the shear stress and first normal stress difference [Figs. 6(a) and 6(b)] that is followed by an additional, long-time sigmoidal relaxation before achieving a plateau. This anomalous behavior has been previously ascribed to formation of shear-banding kinematics [14]. Indeed, this startup behavior has transient rheology comparable to that reported by Hu and Lips [4], who measured the flow kinematics for a similar composition at a comparable Weissenberg number ($Wi = \dot{\gamma}\lambda$).

In contrast to startup flow in region I, for this condition in region II a prominent stress overshoot is observed, which ends abruptly at $t \approx \lambda$ and is followed by a metastable state of nearly homogeneous flow that persists until $t < 6\lambda$. During this metastable state, the 2D SANS patterns for both positions show strong flow alignment that is nearly identical for both spatial positions. Kinematic measurements also show that the shear rate is homogenous across the flow field during this part of the transient [4]. The corresponding order parameters $|A_f|$ and ϕ_0 are observed to evolve equally in both positions in the gap as seen in Figs. 6(c) and 6(d), with plateau values $A_{f,\text{plateau}} = 0.318 \pm 0.029$ and $\phi_{0,\text{plateau}} = 5.3^\circ \pm 0.9^\circ$. At $t \sim 6\lambda$ the microstructures in the inner and outer regions of the gap evolve differently. We identify this point as the *onset of shear banding*, after which the material shearing in the inner (high-shear) band aligns further, whereas the material shearing in the outer (low-shear) band relaxes and becomes more isotropic. This is illustrated in the schematic in Fig. 5 (upper panel). This second transient evolves until $t \sim 2\lambda_{\text{rep}}$, where $\lambda_{\text{rep}} = 9.2 \text{ s}$ is the reptation time, after which a second plateau in $|A_f|$ and ϕ_0 is observed in both bands, which marks the achievement of steady shear banding. The 2D patterns for the inner- and outer-gap spatial positions visually illustrate a large difference in flow alignment at steady state (Fig. 5) that corresponds to shear-banding flow.

The circularly averaged intensities shown in Fig. 5 show distinct differences with time at lower values of scattering vector magnitude q . Specifically, an upturn at low q that indicates the formation of shear-induced concentration fluctuations is evident for SANS patterns that show strong flow alignment. This upturn corresponds with the existence of strongly anisotropic, depolarized light scattering, as is observed in Fig. 5 (upper panel). The existence of butterfly

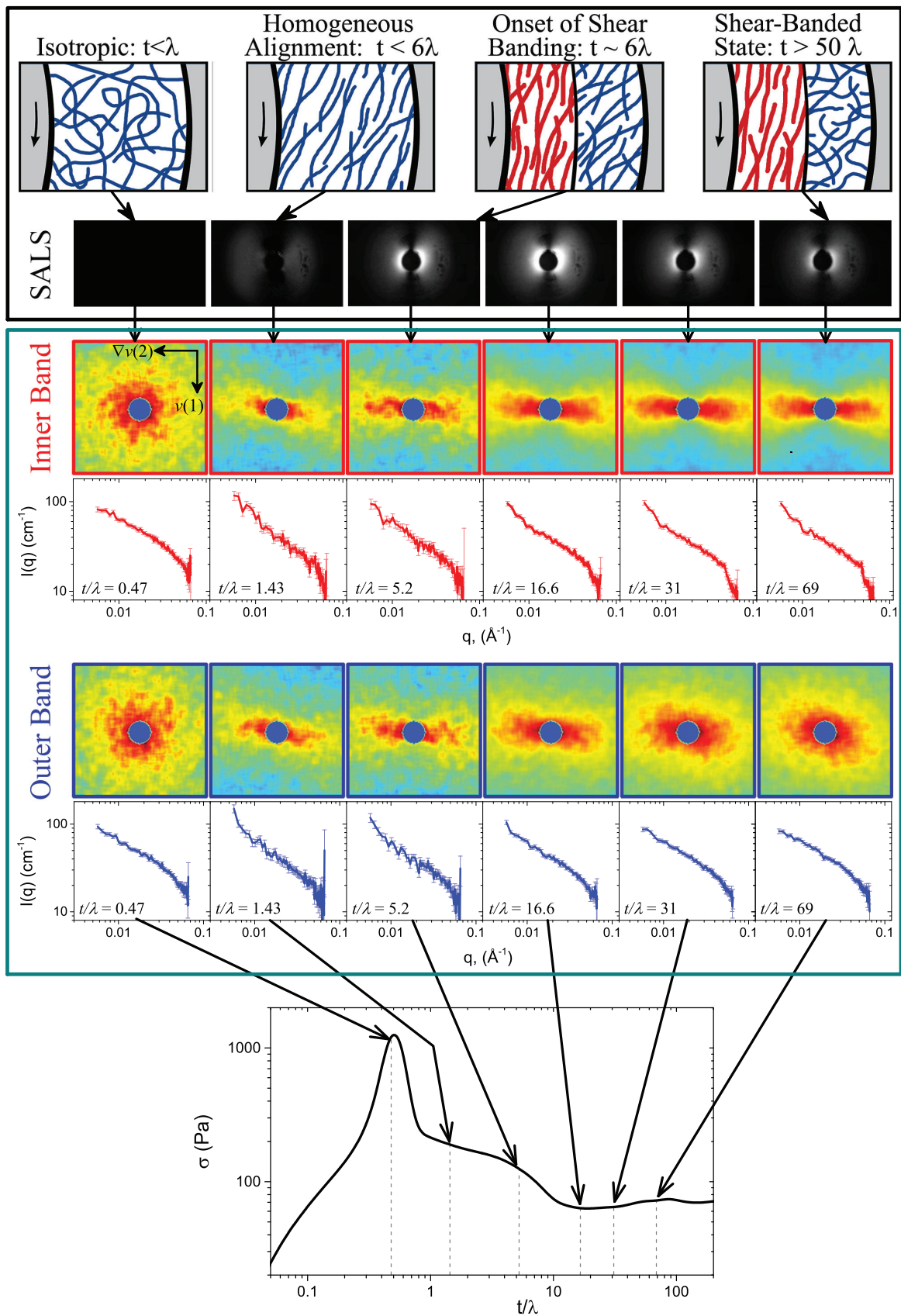


FIG. 5. (Color online) Shear startup at $\dot{\gamma} = 22 \text{ s}^{-1}$: The upper panel shows a schematic of the microstructure with corresponding SALS patterns [40], the middle panel shows 2D SANS patterns and the corresponding $\langle I(q) \rangle$ for the inner ($r/H = 0.2$) and outer ($r/H = 0.8$) spatial positions, and the lower panel shows the shear stress versus time.

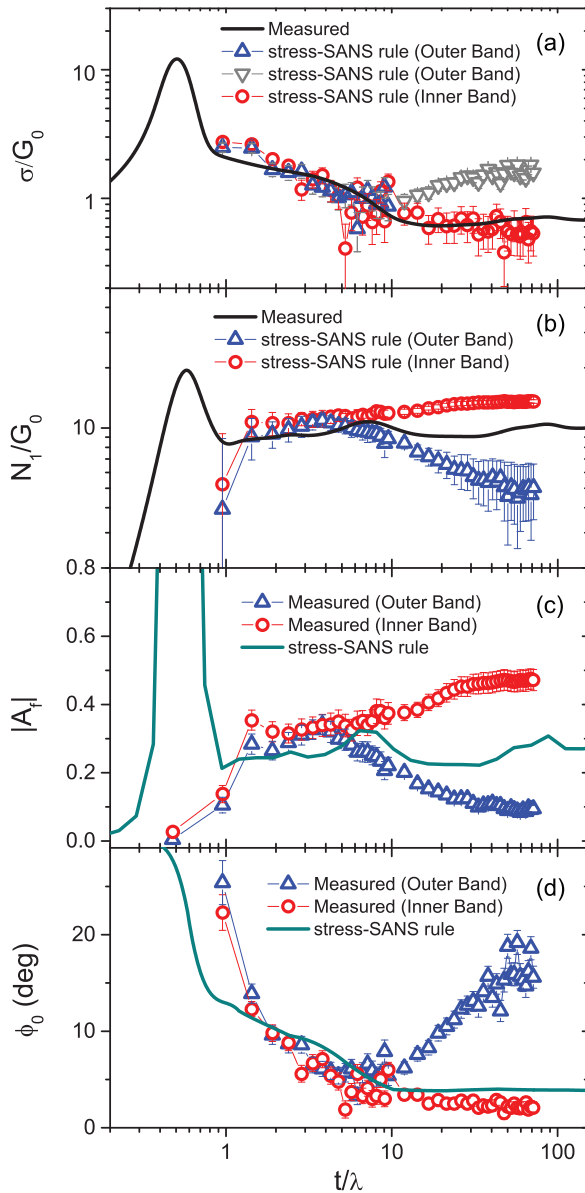


FIG. 6. (Color online) Shear startup at $\dot{\gamma} = 22 \text{ s}^{-1}$: (a) shear stress and (b) first normal stress difference. The solid lines are rheological measurements and symbols are predictions via the stress-SANS rule (with $C_1 = 112$) and data of $|A_f|$ and ϕ_0 , with measured values shown in (c) and (d), respectively. For (c) and (d) the lines are calculations of the respective order parameters using the stress-SANS rule and the measured rheology.

patterns in light scattering is a signature of shear-induced concentration fluctuations that are sometimes observed in the highly nonlinear flow regime (region III) of similar WLM solutions [15]. The scattering at lower q evident in depolarized light scattering (Fig. 5) corresponds to longer length scale (on the order of $1 \mu\text{m}$ and longer) concentration and orientation fluctuations along the flow direction [29]. Finally, returning to the SANS spectra, the consistent shape for high- q values shows that the micellar state of aggregation into wormlike micelles is not affected by the flow.

The stress-SANS rule is violated far from equilibrium due to nonlinearities such as those leading to the butterfly

scattering in SALS such that the stress-SANS coefficient becomes shear rate dependent, i.e., $C_1(\dot{\gamma})$ for $\dot{\gamma} > \dot{\gamma}_{lc}$ [13]. From steady shear measurements at $\dot{\gamma} = 22 \text{ s}^{-1}$ we empirically determine $C_1 = 112$ [47]. This value is used for the prediction of the shear and first normal stress differences shown in Figs. 6(a) and 6(b) and for the reverse prediction of the order parameters from the rheology in Figs. 6(c) and 6(d). An accurate and quantitative relationship between the temporal evolution of the shear stress and the local microstructures in both bands is observed in the metastable state prior to banding, as well as for the high-shear band after the onset of shear banding. This confirms the hypothesis that during flow startup and after the initial stress overshoot, the WLM solution is flow aligned and disentangled, corresponding to a microstructure consistent with the high-shear rate branch of the underlying constitutive equation. Alternatively, A_f and ϕ_0 can be successfully calculated from the measured values of σ and N_1 , as shown in Figs. 6(c) and 6(d) highlighting the quantitative coupling between the micellar orientation order and macroscopic material functions during transient flow (as previously shown for steady shear [13]).

Not surprisingly, however, using this empirical nonlinear stress-SANS coefficient $C_1 = 112$ produces a poor prediction of the shear stress in the evolving low-shear band [see gray triangles in Fig. 6(a)]. As the formation of the low-shear band is hypothesized to be the re-entanglement of the WLM solution, using the linear stress-SANS coefficient $C_1 = 11.2$ should (and does) quantitatively predict the measured shear stress (Fig. 7). Thus, the evolving low-shear band is accurately described as a shearing but entangled PLM (flowing at $\dot{\gamma} \sim \dot{\gamma}_{lc}$ [26,48]) with a microstructure typical of the low-shear branch of the constitutive equation. These results provide a quantitative validation of the hypothesis by Hu *et al.* that the formation of the kink-banded state proceeds by the reentanglement of the PLM flowing near the outer wall, as inferred from observations of the reduction in the local shear rate [4,25].

The initial stress overshoot corresponds to an elastic response, which, as shown in Fig. 2, scales with strain, however, no shear banding is observed in either our SANS measurements or the reported velocity field measurements

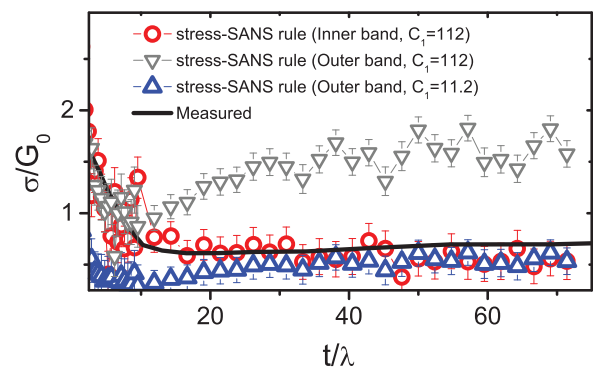


FIG. 7. (Color online) Shear startup at $\dot{\gamma} = 22 \text{ s}^{-1}$: shear stress compared with predictions via the stress-SANS rule and the measured order parameters shown in Figs. 6(c) and 6(d) using the linear stress-SANS coefficient $C_1 = 11.2$ for the outer band for $t/\lambda > 5$ and the nonlinear coefficient $C_1 = 112$ for rest of the conditions, as shown in Fig. 6.

[4,28]. Rather, the abrupt stress reduction immediately after the peak stress is followed by the homogeneous shearing of an aligned, disentangled PLM for times of $t \sim 5 - 6\lambda$, whereupon a stress decrease and subsequent oscillations signal the evolution of a shear-banded flow. One-dimensional linear stability analysis shows the possibility of shear banding commencing at or even just prior to a stress maximum [31], which is not observed at the first stress overshoot but rather appears after the second stress reduction. The onset of banding is consistent with expectations for a viscous type-I banding instability [37]. Now, with our local microstructure measurements and the quantitative determination of the stress-SANS coefficients, we can definitively identify the sequence of events leading to the formation of the banded state. Following the abrupt drop in viscosity, the homogeneous metastable fluid is somewhat flow aligned and corresponds to the high-shear rate branch (region III). The quantitative failure of the linear stress-SANS rule for the high-shear band near equilibrium corresponds with the observation of a butterfly pattern in the rheo-SALS measurement and an upturn in the SANS $\langle I(q) \rangle$ at low q , which signals flow-induced heterogeneities on the micron length scale [4,17,49,50]. Weak butterfly SALS patterns are evident after the stress overshoot (see upper panel in Fig. 5) and oscillations in the butterfly SALS pattern intensities are observed at intermediate times ($\lambda < t < 25\lambda$), after which a steady intensity is observed that is coincident with the onset of the steady-banded state (a movie displaying the temporal evolution of the SALS pattern is shown in the Supplemental Material [40]). Thus, we identify this behavior as a type-I banding instability accompanied by shear-induced concentration fluctuations [5].

Our measurements confirm that the long transient observed in the third stage of the startup is governed by reentanglement of the shearing micelles in the low-shear band that is commensurate with the acceleration of the disentangled, shear-demixed material in the high-shear band. Hence, we confirm that the high-shear band (and the high-shear region in general) is not a shear-induced nematic phase [14] but rather a low-viscosity, partially-flow-aligned PLM phase as argued previously [4]. Plots of $\langle I(q) \rangle$ for all of these microstructural states are shown in Fig. 5, where it can be seen that the PLM state of aggregation as wormlike chains is always observed, but strong forward scattering is evident in the SANS data that portends the spatial concentration heterogeneities observed optically. Furthermore, our observations of the different stress-SANS coefficients for the two bands is consistent with strong nonlinear stretching and alignment in the high-shear band and not micellar scission, which would lead to a dramatic reduction in the stress-SANS coefficient as opposed to the dramatic increase observed here [51]. These detailed observations of the kinetics of the microstructure evolution during banding will be used to further quantitatively test microstructural-based theories of shear banding [30].

The prior reports of spatiotemporal resolved flow birefringence by Lee *et al.* [14,29] measured strong flow birefringence for a different composition (4.4 wt. %, in de-ionized water) and also show that fluctuations in concentration also form along the flow direction in the high-shear band, consistent with the butterfly SALS patterns [15]. The large fluctuations in flow birefringence observed in the shear-banding states were taken

as evidence that shear-induced demixing is responsible for the shear banding for this composition, which is relatively far from the isotropic-nematic transition. This conclusion is consistent with our observations and a similar sequence of events is observed during flow startup, in qualitative support of the proposed scenario of Hu and Lips. Other reports of birefringence and flow-induced NMR quadrupole broadening [27] in the high-shear band for more concentrated PLM solutions under shear strongly indicate the possible formation of a nematic phase that nucleates in the high-shear region and leads to band formation. However, these observations are for a significantly more concentrated PLM solution (10%) for which the banding is also unstable [27,29,44]. Berret and co-workers showed that the stress plateau dramatically flattens and the transitions with shear rate sharpen with increasing surfactant concentration, i.e., as the composition increases towards the equilibrium isotropic-nematic phase transition [14]. Thus, by comparison of this literature with our results, we can deduce that for this system comprised of long, threadlike micelles, increasing surfactant concentration ultimately leads to a loss of stability of the high-shear band in the stress plateau that is associated with a transition in mechanism from shear banding due to the disentanglement-entanglement process to shear banding driven by paranematic formation. This behavior is consistent with model predictions that also suggest a transition from shear banding to vorticity banding [20]. Note that previous 1-2 plane flow-SANS measurements have demonstrated that for systems where shear banding leads to nematic order in the high-shear band, a shear-induced concentration gradient is also created where the high-shear band is enriched in surfactant at the expense of the low-shear band, in agreement with theory [18,19]. Our SANS measurements show no measurable concentration gradients for this system in the banding state, further confirming the disentanglement-reentanglement process as underlying shear banding for the surfactant composition probed here [47]. This may not be surprising given the significant concentration difference between this sample (6 wt. %) and the nematic phase (23 wt. %).

B. Relaxation experiments

Figure 8 shows σ/G_0 and $|A_f|$ as a function of time during relaxation after cessation of steady shear. Upon cessation of the homogeneous flow ($\dot{\gamma} = 2.2 \text{ s}^{-1}$), σ relaxes with the characteristic relaxation time of the equilibrium fluid, i.e., $\sigma \sim \exp(-t/\lambda)$. On the other hand, the stress decay from a shear-banding state ($\dot{\gamma} = 22 \text{ s}^{-1}$) clearly exhibits a significant and fast relaxation followed by a longer relaxation similar to that observed for the lower shear rate. Two distinct relaxations can be modeled as two exponential decays with decay constants 3λ for $t < \lambda$ and λ for $t \geq \lambda$. Interestingly, this anomalous stress decay at shorter times occurs without a corresponding relaxation in the segmental orientation or alignment, i.e., without decay in A_f [see Fig. 8(b)]. Thereafter, the microstructures in both the high- and low-shear bands relax, i.e., the values of A_f decrease, with the same time constant as the stress.

The initial *delay* of the segmental relaxation is associated with a relaxation of the density fluctuations on the micron scale, as observed by the disappearance of the butterfly

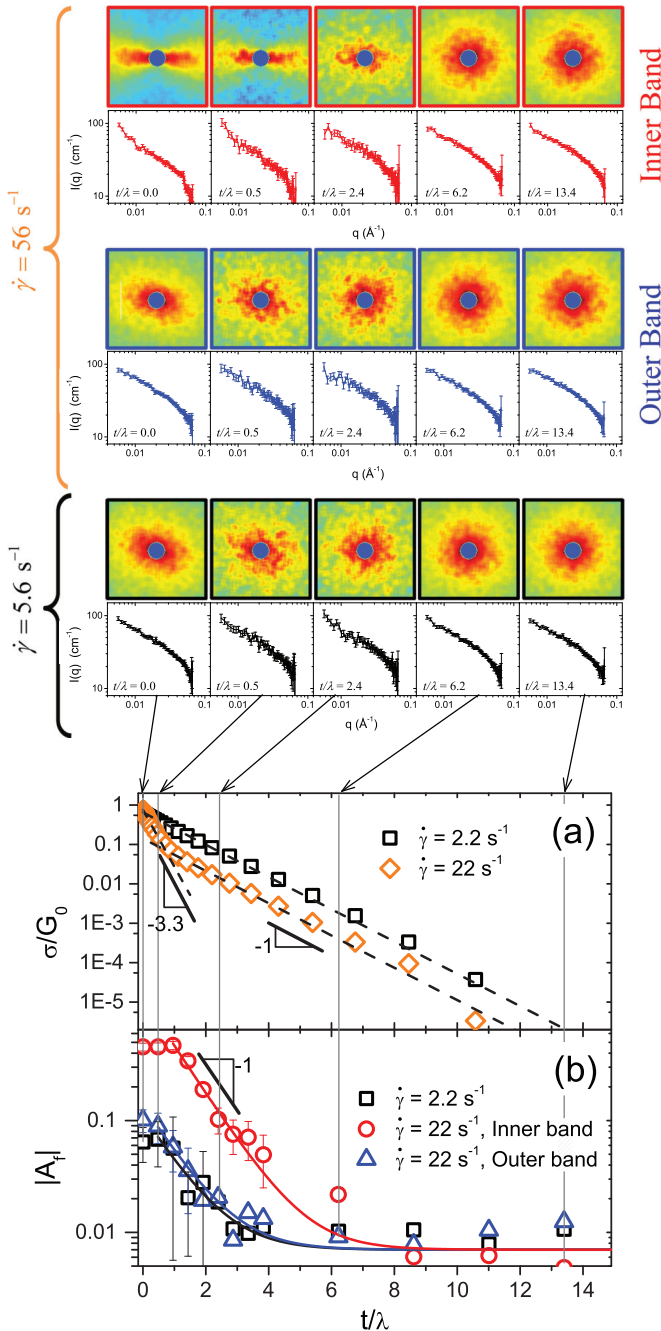


FIG. 8. (Color online) Stress relaxation experiments: The upper panel shows 2D SANS patterns and the corresponding $\langle I(q) \rangle$ plots and the lower panel shows the evolution of (a) stress and (b) $|A_f|$ after shear cessation. Dashed lines in (a) are fits to a single-exponential decay for relaxation from $\dot{\gamma} = 2.2 \text{ s}^{-1}$ and to two exponential decays for relaxation from $\dot{\gamma} = 22 \text{ s}^{-1}$. Solid lines in (b) are fits to a single-exponential decay function $|A_f| \sim \exp(-t/\lambda) + |A_f|_\infty$, with an offset $|A_f|_\infty = 0.007$.

SALS profiles upon shear cessation. A movie available in the Supplemental Material shows the evolution of SALS profiles during shear startup and cessation [40]. Small-angle light scattering measurements during relaxation show a butterfly pattern at time $t = 0$, which disappears in less than 0.5λ ; a similar behavior is seen in the low- q scattering SANS (Fig. 8, upper panel). These observations help explain the

anomalous stress relaxation from the banded state; namely, the high-shear band undergoes an initial relaxation of the large density fluctuations (accompanied by a large reduction in stress), which is then followed by the expected relaxation of micelle orientation on the segmental length scale, with characteristic time λ , and the associated relaxation in the stress arising from the segmental orientation. These observations help clarify the importance of the longer-length-scale density fluctuations evident in SALS in determining the stress in region III and the high-shear band in region II. The rapid stress relaxation observed for relaxation from the shear-banding state corresponds to the relaxation of the shear-induced density fluctuations, which provide the dominant contribution to the stress. Thus, the larger value of the stress-SANS coefficient in the nonlinear regime reflects this additional stress contribution as not all of the stress arises from the micellar microstructure on the segmental length scale, but rather significant contributions arise from longer-length-scale structures.

IV. CONCLUSION

In summary, we have presented the results of a stroboscopic spatiotemporal-resolved SANS technique (1-2 stroboscopic flow SANS) that enables measuring microstructural changes directly in the plane of shear flow [34]. Using this method, we elucidated the quantitative relation between the local spatiotemporally evolving microstructure in the plane of shear and the rheology during startup shear for solutions of long, threadlike micelles in both weakly nonlinear shear flow and highly nonlinear shear-banding flow. This enables definitively identifying the mechanism by which stable shear banding forms in highly entangled polymerlike micellar solutions. Namely, after an initial elastic response and significant stress overshoot, a transient, low-viscosity, flow-aligned (disentangled) PLM solution persists and eventually evolves to a stable shear-banded flow by the formation of a low-shear band of nearly isotropic (entangled) viscous WLM solution. Through comparison to literature studies on similar but more concentrated solutions, we deduced that unstable banding is likely due to shear-induced nematic formation as compositions tend towards that of the underlying, equilibrium isotropic-nematic phase transitions.

The linear stress-SANS rule quantitatively predicts the transient stress for shear rates in region I. For shear rates corresponding to the stress plateau, this linear stress-SANS rule also quantitatively predicts the properties of the low-shear band, confirming it to be a near-equilibrium entangled micellar solution. However, an empirical, nonlinear stress-SANS coefficient is required to quantitatively predict the rheology of the transient state and the evolving high-shear band evident during shear startup. The nonlinear stress-SANS coefficient is substantially larger than the linear value and this certainly reflects additional contributions to the stress from the long-length-scale structure evident in the butterfly scattering patterns. This was confirmed by examination of the stress relaxation, where a significant stress relaxation accompanies decay of the butterfly scattering in SALS without commensurate change in the SANS order parameters.

These measurements in the 1-2 plane of flow definitively show how nonlinear startup flow evolves through a metastable,

homogeneous flow into a kink shear band over many relaxation times. Each band has a distinctly different level of segmental orientation and alignment corresponding to those observed in regions I and III of the steady-state flow curve. We further confirmed the predicted type-I shear banding as predicted for such complex fluids and provided a quantitative understanding of the complex time-dependent rheology in terms of the evolving underlying microstructure of the complex fluid. Therefore, these quantitative data should be invaluable for the development and validation of improved constitutive models for complex fluids in nonlinear flows.

ACKNOWLEDGMENTS

This paper was prepared under cooperative Agreements No. 70NANB7H6178 and No. 70NANB10H256 from the National Institute of Standards and Technology, US Department of Commerce. The statements, findings, conclusions and recommendations are those of the authors and do not necessarily reflect the view of NIST or the U.S. Department of Commerce. The Institut Laue Langevin (Grenoble, France) is acknowledged for the beam time allocated on D22.

-
- [1] J. D. Goddard, *Annu. Rev. Fluid Mech.* **35**, 113 (2003).
- [2] T. C. B. McLeish and R. G. Larson, *J. Rheol.* **42**, 81 (1998).
- [3] C. Grand, J. Arrault, and M. E. Cates, *J. Phys. II (France)* **7**, 1071 (1997).
- [4] Y. T. Hu and A. Lips, *J. Rheol.* **49**, 1001 (2005).
- [5] N. A. Spenley, M. E. Cates, and T. C. B. McLeish, *Phys. Rev. Lett.* **71**, 939 (1993).
- [6] H. Rehage and H. Hoffmann, *Mol. Phys.* **74**, 933 (1991).
- [7] M. E. Cates and S. J. Candau, *J. Phys.: Condens. Matter* **2**, 6869 (1990).
- [8] J.-F. Berret, G. Porte, and J.-P. Decruppe, *Phys. Rev. E* **55**, 1668 (1997).
- [9] E. Cappelaere, R. Cressely, and J. P. Decruppe, *Colloid. Surf. A* **104**, 353 (1995).
- [10] E. Cappelaere, J. F. Berret, J. P. Decruppe, R. Cressely, and P. Lindner, *Phys. Rev. E* **56**, 1869 (1997).
- [11] S. Lerouge, J. P. Decruppe, and C. Humbert, *Phys. Rev. Lett.* **81**, 5457 (1998).
- [12] S. Lerouge, J. P. Decruppe, and J. F. Berret, *Langmuir* **16**, 6464 (2000).
- [13] M. E. Helgeson, P. A. Vasquez, E. W. Kaler, and N. J. Wagner, *J. Rheol.* **53**, 727 (2009).
- [14] J.-F. Berret, *Langmuir* **13**, 2227 (1997).
- [15] I. A. Kadoma and J. W. van Egmond, *Langmuir* **13**, 4551 (1997).
- [16] M. W. Liberatore, F. Nettekheim, N. J. Wagner, and L. Porcar, *Phys. Rev. E* **73**, 020504 (2006).
- [17] P. Thareja, I. H. Hoffmann, M. W. Liberatore, M. E. Helgeson, Y. T. Hu, M. Gradzielski, and N. J. Wagner, *J. Rheol.* **55**, 1375 (2011).
- [18] M. E. Helgeson, M. D. Reichert, Y. T. Hu, and N. J. Wagner, *Soft Matter* **5**, 3858 (2009).
- [19] M. E. Helgeson, L. Porcar, C. Lopez-Barron, and N. J. Wagner, *Phys. Rev. Lett.* **105**, 084501 (2010).
- [20] M. E. Cates and S. M. Fielding, *Adv. Phys.* **55**, 799 (2006).
- [21] J. K. G. Dhont, *Phys. Rev. E* **60**, 4534 (1999).
- [22] S. Lerouge and J.-F. Berret, in *Polymer Characterization*, edited by K. Dusek, and J.-F. Joanny (Springer, Berlin, 2010), pp. 1.
- [23] P. D. Olmsted, *Rheol. Acta* **47**, 283 (2008).
- [24] S. Lerouge, M. A. Fardin, M. Argentina, G. Gregoire, and O. Cardoso, *Soft Matter* **4**, 1808 (2008).
- [25] Y. T. Hu, C. Palla, and A. Lips, *J. Rheol.* **52**, 379 (2008).
- [26] M. M. Britton and P. T. Callaghan, *Phys. Rev. Lett.* **78**, 4930 (1997).
- [27] M. R. López-González, W. M. Holmes, P. T. Callaghan, and P. J. Photinos, *Phys. Rev. Lett.* **93**, 268302 (2004).
- [28] E. Miller and J. P. Rothstein, *J. Non-Newton. Fluid Mech.* **143**, 22 (2007).
- [29] J. Y. Lee, G. G. Fuller, N. E. Hudson, and X.-F. Yuan, *J. Rheol.* **49**, 537 (2005).
- [30] N. Germann, L. P. Cook, and A. N. Beris, *J. Non-Newton. Fluid Mech.* **196**, 51 (2013).
- [31] R. L. Moorcroft and S. M. Fielding, *Phys. Rev. Lett.* **110**, 086001 (2013).
- [32] C. J. Pipe, N. J. Kim, P. A. Vasquez, L. P. Cook, and G. H. McKinley, *J. Rheol.* **54**, 881 (2010).
- [33] S. Manneville, *Rheol. Acta* **47**, 301 (2008).
- [34] A. K. Gurnon, P. R. Eberle, L. Porcar, P. D. Butler, and N. J. Wagner, *J. Visual Exp.* **84**, e51068 (2014).
- [35] A. P. R. Eberle and L. Porcar, *Curr. Opin. Colloid Interface Sci.* **17**, 33 (2012).
- [36] J. P. Decruppe, S. Lerouge, and J. F. Berret, *Phys. Rev. E* **63**, 022501 (2001).
- [37] S. M. Fielding and P. D. Olmsted, *Phys. Rev. E* **68**, 036313 (2003).
- [38] P. A. Vasquez, G. H. McKinley, and L. P. Cook, *J. Non-Newton. Fluid Mech.* **144**, 122 (2007).
- [39] H. Rehage and H. Hoffmann, *J. Phys. Chem.* **92**, 4712 (1988).
- [40] See Supplemental Material at <http://link.aps.org/supplemental/10.1103/PhysRevE.89.042301> for a description of rheological characterization, SANS plots, and a movie showing the time evolution of the SALS patterns.
- [41] C. R. López-Barrón and N. J. Wagner, *Soft Matter* **7**, 10856 (2011).
- [42] A. K. Gurnon, C. R. López-Barrón, A. P. R. Eberle, L. Porcar, and N. J. Wagner, *Soft Matter* **10**, 2889 (2014).
- [43] C. R. López-Barrón, L. Porcar, A. P. R. Eberle, and N. J. Wagner, *Phys. Rev. Lett.* **108**, 258301 (2012).
- [44] M. P. Lettinga and S. Manneville, *Phys. Rev. Lett.* **103**, 248302 (2009).
- [45] L. M. Walker and N. J. Wagner, *Macromolecules* **29**, 2298 (1996).
- [46] R. B. Bird, *Dynamics of Polymeric Liquids*, 2nd ed. (Wiley, New York, 1987).
- [47] A. K. Gurnon, C. R. López-Barrón, M. J. Wasbrough, L. Porcar, and N. J. Wagner, *ACS Macro Lett.* **3**, 276 (2014).

- [48] J.-B. Salmon, A. Colin, S. Manneville, and F. Molino, *Phys. Rev. Lett.* **90**, 228303 (2003).
- [49] J. Bastide, L. Leibler, and J. Prost, *Macromolecules* **23**, 1821 (1990).
- [50] I. Kadoma, C. Ylitalo, and J. Egmond, *Rheol. Acta* **36**, 1 (1997).
- [51] M. Doi and S. F. Edwards, *The Theory of Polymer Dynamics* (Clarendon, New York, 1986), Vol. 73.